



CHORUS

This is the accepted manuscript made available via CHORUS. The article has been published as:

Double transverse wave-vector correlations in photon pairs generated by spontaneous parametric down-conversion pumped by Bessel-Gauss beams

Verónica Vicuña-Hernández, José T. Santiago, Yasser Jerónimo-Moreno, Roberto Ramírez-Alarcón, Héctor Cruz-Ramírez, Alfred B. U'Ren, and Rocio Jáuregui-Renaud

Phys. Rev. A **94**, 063863 — Published 30 December 2016

DOI: [10.1103/PhysRevA.94.063863](https://doi.org/10.1103/PhysRevA.94.063863)

Double transverse wavevector correlations in photon pairs generated by spontaneous parametric down conversion pumped by Bessel-Gauss beams

Verónica Vicuña-Hernández¹, José T. Santiago¹, Yasser Jerónimo-Moreno², Roberto Ramírez-Alarcón³, Héctor Cruz-Ramírez¹, Alfred B. U'Ren^{1*}, Rocio Jauregui-Renaud²

¹*Instituto de Ciencias Nucleares, Universidad Nacional Autónoma de México,*

Apdo. Postal 70-543, 04510 Cd. de México, México

²*Instituto de Física, Universidad Nacional Autónoma de México,*

Apdo. Postal 20-364, 01000 Cd. de México, México

³*Centro de Investigaciones en Optica A.C., Loma del Bosque 115, Colonia Lomas del Campestre, 37150 León Guanajuato, México*

We present an experimental and theoretical study of type I, frequency-degenerate spontaneous parametric downconversion (SPDC) with a Bessel-Gauss pump in which we include, both, paraxial and non-paraxial pump beam configurations. We present measurements of the SPDC angular spectrum (AS), of the conditional angular spectrum (CAS) of signal-mode single photons as heralded by the detection of an idler photon, and of the transverse wavevector signal-idler correlations (TWC). We show that as the pump is made increasingly non-paraxial the AS acquires a non-concentric double-cone structure, with the CAS shape depending on the azimuthal location of the heralding detector, while the signal-idler wavevector correlation region splits into characteristic doublet stripes, representing as yet unexplored non-trivial, non-local quantum correlations between the signal and idler photons. Our work provides further understanding of SPDC with a particular class of structured pump beams, and we believe that the controlled presence of double wavevector correlations represents an interesting new resource for photon-pair quantum state engineering.

PACS numbers: 42.50.-p, 42.50.Dv, 03.65.Ud

I. INTRODUCTION

The study and generation of spatially structured beams has gained huge importance in a number of fields, including micro-manipulation [1–3], as well as linear [4, 5] and nonlinear [6–8] optics and microscopy [9]. Bessel-Gauss beams are characterized by some particularly interesting properties: i) they are propagation-invariant [10], ii) they may exhibit optical vortices [11, 12] and non-local correlations in orbital angular momentum (OAM) [13, 14], iii) they have self-healing attributes implying that they may reconstruct following the presence of an obstacle [15], and iv) they are turbulence-invariant [16]. It has been predicted [17, 18] and experimentally observed [19–21] that the generation of photon pairs with similar characteristics ‘inherited’ from the pump can be achieved through the process of spontaneous parametric down-conversion (SPDC) using as pump a Bessel-Gauss beam. The resulting photons possess the properties i) through iv) above, besides transverse wavevector quantum correlations with an unusual topology that could make them especially attractive for the implementation of quantum protocols.

In this work we report a careful experimental study of photon pairs generated through a type I SPDC process employing a negative uniaxial nonlinear crystal with a zeroth order Bessel-Gauss (BG) beam as pump. The high quality of the pump beam was ascertained by measuring its angular spectrum, which exhibits a high degree of cylindrical symmetry and is well characterized by the value of its mean transverse wavenumber κ_{\perp} and corresponding width $\delta_{\kappa_{\perp}}$ (see below). The experimental

and theoretical study here reported assumes normal incidence of the pump beam on the crystal with κ_{\perp} values, both, within and outside of the paraxial regime. In the latter case, birefringence effects such as *walkoff* can be observed, and new effects can also arise in the nonlinear optics realm. The meticulous preparation of the pump beam in our experiment allows the observation of a number of interesting properties of the photon pairs generated in the SPDC process. In particular, we study the appearance of a non-concentric double-cone emission structure [19, 22], in contrast with the single cone which characterizes SPDC sources based on a Bessel-Gauss pump with a small κ_{\perp} value ($\kappa_{\perp} \leq \delta_{\kappa_{\perp}} \ll \omega/c$), which includes Gaussian-beam pumps in the limit $\kappa_{\perp} \rightarrow 0$. Our study shows that photon pairs can be emitted with an easily-controllable azimuthal asymmetry that depends on the value of κ_{\perp} : the probability of detecting a photon pair has the highest values within a well-defined region of the transverse plane. This asymmetry, in the non-paraxial regime for the pump, leads also to the generation of heralded photons described by superpositions of stationary Bessel modes of different orders, as dependent on the azimuthal angle of detection [22]. Meanwhile, in the paraxial regime the spatial structure of the photon pairs is directly inherited from the pump beam as is known from previous works [17–19, 22–25].

In this paper we report novel results for the correlations in the $x-x$, $x-y$ and $y-y$ transverse wavevector components of the photon pairs in both the paraxial and non-paraxial regimes [26–28]. In the first regime a diagonal stripe in the space formed by k_a^s and k_b^i , where a and b can take the values x and y , correlates the wavevec-

tors for the signal and idler photons. While the width of this stripe is determined by the wavevector spread $\delta_{\kappa_{\perp}}$, its length is determined by the crystal properties, and in particular by its length. As the pump beam departs from the paraxial regime, this stripe splits into characteristic doublet stripes compatible with the double-cone structure of the SPDC angular spectrum. That is, each k_a^s value is strongly correlated with a pair of k_b^i values (with $a = b$). To the best of our knowledge, these double correlations have not been studied before; they undoubtedly constitute a resource for the controlled generation of photon pairs entangled in continuous variables with a particularly non-trivial topology.

II. TYPE I SPDC WITH A BESSEL-GAUSS PUMP

In general, the SPDC photon-pair properties have as control parameters: i) the crystal characteristics including dimensions, orientation of optic axes, and spatial variation of the nonlinear electric susceptibility, and ii) the pump characteristics, in particular its spatial and temporal structure. In previous papers, we have studied type I SPDC with a Bessel-Gauss pump beam from the theoretical point of view [22], and, for relatively low values of κ_{\perp} , also from the experimental point of view [19–21]. We note that in the literature, most SPDC work involves the use of paraxial pump beams. In this paper we extend our experimental study to also include: i) pump beams outside of the paraxial regime, and ii) measurements of the wavevector signal-idler correlations. Our analysis relies on electromagnetic modes which fulfill Maxwell's equations strictly, so that it applies both within and outside of the paraxial regime. We will focus on spectrally-degenerate SPDC—both photons are centered around the same frequency—with non-collinear emission.

Consider a continuous, quasi-monochromatic, and coherent pump beam of amplitude α_p and frequency ω_p that impinges on a wide (as compared to the pump transverse dimensions) nonlinear crystal of length L , with its main propagation direction parallel to the normal of the crystal surfaces, defined as the Z -axis. The quantum state of the electromagnetic field related to the SPDC process at asymptotic times is given by

$$|\Psi\rangle = |0; \alpha_p\rangle + \frac{\pi}{i\hbar} \int d\omega^s \alpha_p \int d^2k_{\perp}^s \int d^2k_{\perp}^i \mathcal{N}_p \mathcal{N}_s \mathcal{N}_i \chi \cdot F(\mathbf{k}_{\perp}^s, \omega^s, \mathbf{k}_{\perp}^i, \omega^p - \omega^s) |0; \alpha_{k^p}; 1_{k^s}; 1_{k^i}\rangle \quad (1)$$

where $\mathcal{N}_{p,s,i}$ represents the normalization factors associated with the pump (p), signal (s) and idler (i) modes, the factor χ is the effective nonlinear electric susceptibility that depends on the particular crystal under consideration, and $F(\mathbf{k}_{\perp}^s, \omega^s, \mathbf{k}_{\perp}^i, \omega^p - \omega^s)$ is the joint amplitude defined as

$$F(\mathbf{k}_{\perp}^s, \omega^s, \mathbf{k}_{\perp}^i, \omega^p - \omega^s) = \psi(\mathbf{k}_{\perp}^s + \mathbf{k}_{\perp}^i) \text{sinc}(L \Delta k_z / 2) \exp(-i L \Delta k_z / 2), \quad (2)$$

where $\Delta k_z = k_z^p - k_z^s - k_z^i$, and where signal (idler) wavevectors are evaluated at frequency ω_s ($\omega_p - \omega_s$). The 0 in the ket $|0; \alpha_{k^p}; 1_{k^s}; 1_{k^i}\rangle$ denotes that the vacuum is not explicitly written for all modes, α_{k^p} is the coherent state of the pump beam, with wvector \mathbf{k}^p , and $1_{k^{s,i}}$ is a single photon state in the signal and idler mode expressed in wavevector space. The joint amplitude includes the incident structure of the pump photons through its angular spectrum $\psi(\mathbf{k}_{\perp}^p)$. For a linearly-polarized zeroth order BG beam, it corresponds to a Gaussian function of the modulus of the transverse component of the wavevector around a given value κ_{\perp} with a width $\delta_{\kappa_{\perp}}$,

$$\psi(\mathbf{k}_{\perp}^p) = e^{-(k_{\perp}^p - \kappa_{\perp})^2 / 2\delta_{\kappa_{\perp}}^2}. \quad (3)$$

Note that this expression reduces for $\kappa_{\perp} \ll \delta_{\kappa_{\perp}}$ to the angular spectrum of a Gaussian beam. We will work, however, in the regime $\kappa_{\perp} \gg \delta_{\kappa_{\perp}}$ which guarantees quasi propagation-invariance and permits a close approximation to an ideal Bessel beam which can be realistically implemented in the laboratory.

The angular spectrum $\psi(\mathbf{k}_{\perp}^p)$, together with the L -dependent longitudinal phasematching term, determines the angular spectra of the idler and signal photons via the strong phasematching condition $\mathbf{k}_{\perp}^s + \mathbf{k}_{\perp}^i = \mathbf{k}_{\perp}^p$, see Eq. (2). We assume that the crystal is uniaxial, with its optic axis specified by vector \mathbf{a} . In the paraxial regime the standard effective dispersion relation for the extraordinary pump beam $k_z^E(\mathbf{k}_{\perp} \sim \mathbf{0}) = n_e \omega / c$ can be assumed, while outside of this regime the dispersion relation takes the form

$$k_z^E(\mathbf{k}_{\perp}, \omega) = -\beta \mathbf{a}_{\perp} \cdot \mathbf{k}_{\perp} + \frac{\omega}{c} n_e \sqrt{1 - \frac{k_{\perp}^2 c^2}{\omega^2}} \eta, \quad (4)$$

$$n_e = \sqrt{\frac{\epsilon_{\perp} \epsilon_{\parallel}}{\epsilon_{\perp} + \Delta \epsilon a_z^2}}, \quad (5)$$

$$\beta = \frac{\Delta \epsilon a_z}{\epsilon_{\perp} + \Delta \epsilon a_z^2}, \quad (6)$$

$$\eta = \frac{1}{\epsilon_{\perp} + \Delta \epsilon a_z^2}, \quad (7)$$

where $\Delta \epsilon = \epsilon_{\parallel} - \epsilon_{\perp}$ is the difference between the ordinary ϵ_{\perp} and extraordinary ϵ_{\parallel} linear permittivities. These permittivities are frequency-dependent so that the ordinary refractive index $n_o = \sqrt{\epsilon_{\perp}}$, and the terms n_e , β , and η , that determine the dispersion relation for extraordinary beams are also frequency-dependent; for quasi plane waves with a polarization along the crystal axis, n_e can be considered as the extraordinary refractive index. Notice that the exact expression, Eq. (4), is anisotropic even for normal incidence and a linearly polarized pump beam. In fact, the parameter β is a measure of the so-called *Poynting vector walkoff*, i. e., the deviation of the energy

flux as given by the Poynting vector with respect to the main direction of propagation of a paraxial beam within the birefringent crystal.

A. Angular spectrum of SPDC from a Bessel-Gauss pump beam.

In general, from the joint amplitude F , the angular spectrum (AS) of the photon pairs can be calculated as

$$R_s(\mathbf{k}_\perp^s) = |g\alpha_p|^2 \int d\omega^s \cdot \int d^2k_\perp^i |F(\mathbf{k}_\perp^s, \omega^s, \mathbf{k}_\perp^i \omega^p - \omega^s)|^2, \quad (8)$$

$$g = \pi \mathcal{N}_p \mathcal{N}_s \mathcal{N}_i \chi / \hbar.$$

It has been shown recently [22] that approximating the function $\text{sinc}(x)$ in the joint amplitude by a Gaussian function $\exp[-(\gamma x)^2]$, with $\gamma = 0.4393$, and taking the limit $\delta_{k_\perp} \rightarrow 0$ with the restriction of a finite pump intensity, yields the following expression for the AS, valid for frequency-degenerate SPDC ($\omega^s = \omega^i = \omega^p/2$) with a BG pump beam

$$R_s(\mathbf{k}_x^s, \mathbf{k}_y^s) \approx$$

$$e^{-\sigma_{AS}^{-2}((\mathbf{k}_\perp^s)^2 - r_{AS}^2)^2} \int_0^{2\pi} e^{-\frac{(\gamma L)^2}{2}(|\mathbf{d}| \kappa_\perp \sin \varphi_p - \tilde{\kappa})^2} d\varphi_p, \quad (9)$$

$$r_{AS}^2 = (1/2) (n_o \omega^p / c)^2 (1 - (n_e / n_o)), \quad (10)$$

$$\sigma_{AS}^{-2} = 2(\gamma L c / n_o \omega^p)^2, \quad (11)$$

$$\tilde{\kappa} = (\omega^p / c)(n_e - n_o) + (2c / n_o \omega^p)(\mathbf{k}_\perp^s)^2, \quad (12)$$

$$\mathbf{d} = \beta \mathbf{a}_\perp + (2c / n_o \omega^p) \mathbf{k}_\perp^s. \quad (13)$$

Note that for a negative uniaxial crystal ($n_e < n_o$) and for a paraxial pump beam, i. e. $\kappa_\perp \ll (\omega^p / c)|n_e - n_o|$, (which includes Gaussian-beam pumps [31] with $\kappa_\perp = 0$ as a special case), the AS is concentrated nearby a cone given by the condition

$$k_\perp^s = (n_o \omega^p / \sqrt{2} c) \sqrt{1 - n_e / n_o} = r_{AS}.$$

Note also that the Gaussian factor multiplying the integral in Eq. (9) is a function of $(\mathbf{k}_\perp^s)^2$, so that σ_{AS} has units of the inverse of length squared, and the cone width is given approximately by $\Delta_{AS} = \sigma_{AS} / r_{AS}$. It becomes clear that, in this regime, the cone aperture in wavevector space, r_{AS} , depends only on the refractive indices evaluated at the pump and SPDC frequencies, $n_o(\omega^p/2)$ and $n_e(\omega^p)$, while the width σ_{AS} depends also on these indices but is also inversely proportional to the crystal length.

As κ_\perp increases, the restriction $k_\perp^s \approx r_{AS}$ is relaxed: the SPDC spatial structure is the result of the superposition of the contributions to the two-photon state from individual pump wavevectors that arrive symmetrically on the crystal front surface, but are not distributed symmetrically with respect to the optic axis. This anisotropy yields structures that are not centered at the origin, but are displaced along the direction of the optic axis. This displacement would be absent if κ_\perp were zero, *e. g.*, for a Gaussian-beam pump. The AS of a BG beam which is outside of the paraxial regime involves two non-homogenous (i.e. with an azimuthally varying width) and non-concentric cones with unequal radii [22]. For a negative birefringent crystal and for $|n_o \omega^p \beta \mathbf{a}_\perp / 2c| \approx r_{AS} \gg \kappa_\perp$, the two cones have a quasi-circular transverse structure with larger (smaller) radius r_+ (r_-), and center defined by the transverse vector $A_+ \hat{\mathbf{a}}_\perp$ ($A_- \hat{\mathbf{a}}_\perp$), with

$$r_\pm \approx r_{AS} - \frac{\kappa_\perp}{2} \left(1 \pm \frac{n_o \omega^p \beta |\mathbf{a}_\perp|}{2c r_{AS}} \mp \frac{\kappa_\perp}{2 r_{AS}} \right), \quad (14)$$

$$A_\pm \approx \mp \frac{\kappa_\perp}{2} \left(1 + \frac{n_o \omega^p \beta |\mathbf{a}_\perp|}{2c r_{AS}} - \frac{\kappa_\perp}{2 r_{AS}} \right). \quad (15)$$

The two emission cones are nearly tangent to each other along the direction defined by the wavevector $\sim (-r_{AS} + \kappa_\perp/2) \hat{\mathbf{a}}_\perp + k_z \hat{\mathbf{e}}_z$. The double conical structure of the AS reflects both the asymmetric distribution of the wavevectors in the incoming Bessel pump beam with respect to the optic axis and effects proportional to the β term arising in the extraordinary-ray dispersion relation. Below, in Fig. 1, we show a schematic of the SPDC source with BG pump used in our experiments.

As the crystal length is increased, the regions where the AS has significant values become smaller and the anisotropy associated with the extraordinary pump beam dispersion relation becomes more evident. It is expected that a similar structure of the AS would be exhibited if other propagation-invariant beams were to be used as pump beams, in particular, higher-order Bessel-Gauss beams.

B. Conditional angular spectrum (CAS) and transverse wavevector correlation (TWC) functions.

The conditional angular spectrum R_c represents the angular spectrum of the signal photon conditioned on the detection of an idler photon with wavevector \mathbf{k}_0^i . For zeroth order BG pump beams, R_c may be expressed as

$$R_c(\mathbf{k}_\perp^s; \mathbf{k}_{\perp 0}^i; \omega^s, \omega_0^i) =$$

$$|g\alpha_p|^2 \mathcal{S}(\mathbf{k}_\perp^s, \mathbf{k}_{\perp 0}^i) \cdot \mathcal{L}(\mathbf{k}_\perp^s, \mathbf{k}_{\perp 0}^i; \omega^s, \omega_0^i), \quad (16)$$

with

$$\omega^s + \omega_0^i = \omega^p \quad (17)$$

$$\begin{aligned} \mathcal{S}(\mathbf{k}_\perp^s, \mathbf{k}_{\perp 0}^i) &= |\psi(\mathbf{k}_\perp^s + \mathbf{k}_{\perp 0}^i)|^2 \\ &= e^{-(\mathbf{k}_\perp^s + \mathbf{k}_{\perp 0}^i)^2 - \kappa_\perp)^2 / \delta_{\kappa_\perp}^2} \end{aligned} \quad (18)$$

$$\mathcal{L}(\mathbf{k}_\perp^s, \mathbf{k}_{\perp 0}^i; \omega^s, \omega_0^i) = \text{sinc}^2(L \Delta k_z / 2). \quad (19)$$

Here we have assumed a monochromatic pump beam and an ideal resolution in the characterization of the idler and signal wavevectors (corresponding in a practical experimental situation to filtering the SPDC photons with a narrow bandpass filter so as to retain only the degenerate photon pairs with frequency $\omega_p/2$).

The signal-idler transverse wavevector correlations, or TWC, are evaluated in terms of the probability of detecting a pair of photons characterized by wavevector components k_a^s and k_b^i while maintaining the complementary components k_c^s and k_d^i at fixed values, where $a, b, c, d = x, y$, with $c \neq a$ and $d \neq b$. For instance, the $x-x$ TWC function is given by $R_c(k_x^s, k_{y0}^i; k_x^i, k_{y0}^s; \omega_0^s, \omega_0^i)$. As we will study below, the topology of photon-pair wavevector correlations for a non-paraxial BG pump beam has an unusual double-correlation structure which may lead to interesting quantum non-local effects.

The structure of R_c shows that the wavevector correlation functions for BG beams are expected to be maximized in regions of the $\mathbf{k}_\perp^{s,i}$ space where the following phasematching conditions are fulfilled

$$|\mathbf{k}_\perp^s + \mathbf{k}_\perp^i| \approx \kappa_\perp \quad (20)$$

$$\Delta k_z \approx 0. \quad (21)$$

The equalities in Eq. (20) and Eq. (21) are approached for smaller values of δ_{κ_\perp} and larger values of the crystal length L , respectively. Note that the condition given by Eq. (20) for Gaussian beams, that is for $\kappa_\perp = 0$, is equivalent to $\mathbf{k}_\perp^s \approx -\mathbf{k}_\perp^i$.

1. Transverse phasematching constraints

In what follows, we study the constraints on the signal and idler transverse wavevectors derived from Eq. (20), in the case of interest for which $\kappa_\perp \gg \delta_{\kappa_\perp}$. There are, in principle, four different types of transverse wavevector correlation measurements: $x-x$, $y-y$, $x-y$, and $y-x$. The symmetry of the joint wavevector amplitude expected for a type-I, frequency-degenerate photon pair source implies that the $x-y$ and $y-x$ measurements yield the same information. It results from Eq. (20) that

(a) The conditional angular spectrum is maximized on a contour given by a circumference of radius κ_\perp centered around $-\mathbf{k}_{\perp 0}^i$.

(b) The $x-y$ TWC function is also maximized on a contour given by a circumference of radius κ_\perp centered around $(-k_{x0}^i, -k_{y0}^s)$. This circumference may yield non-local Bessel-like photons similar to those reported in Ref. [29].

(c) The $x-x$ TWC function is maximized on contours defined by two lines with a slope of negative unity, $k_x^s = -k_x^i \pm \sqrt{\kappa_\perp^2 - (k_{y0}^s + k_{y0}^i)^2}$, whenever $\kappa_\perp \geq |k_{y0}^s + k_{y0}^i|$.

(d) The $y-y$ TWC function, analogously to (c), is maximized on contours defined by two lines with slope of negative unity, $k_y^s = -k_y^i \pm \sqrt{\kappa_\perp^2 - (k_{x0}^s + k_{x0}^i)^2}$, whenever $\kappa_\perp \geq |k_{x0}^s + k_{x0}^i|$.

It is important to point out that the structure of the doublet stripes appearing in the $x-x$ and $y-y$ TWC functions can be controlled by the source parameters. In particular, the separation of the stripes in transverse wavevector space is determined by κ_\perp as is clear from the above discussion. Likewise, as can be verified through numerical simulations, the width of the stripes is controlled in part by the BG cone width parameter δ_{κ_\perp} , and their length by the crystal thickness L .

2. Longitudinal phasematching constraints

In the case of frequency-degenerate type I SPDC, the approximate conservation of the z wavevector component, Eq. (21), can be written as

$$\Delta k_z \approx \tilde{\kappa} - \mathbf{d} \cdot (\mathbf{k}_\perp^s + \mathbf{k}_\perp^i) \approx 0. \quad (22)$$

This expression results from the first-order Taylor expansion of the extraordinary-ray dispersion relation, Eq. (4), in $\kappa_\perp c / \omega^p$ and the strong phasematching condition for the transverse wavevectors. The width of the distribution associated with this phasematching condition decreases linearly with the crystal length. A direct calculation shows that the fulfilment of Eqs. (20) and (22) implies the following condition

$$\begin{aligned} \left| \mathbf{k}_\perp^s - \frac{n_o \omega^p}{2c} \beta \mathbf{a}_\perp \right|^2 + \left| \mathbf{k}_\perp^i - \frac{n_o \omega^p}{2c} \beta \mathbf{a}_\perp \right|^2 \approx \\ 2r_{AS}^2 + \kappa_\perp^2 + \left(\frac{n_o \omega^p \beta |\mathbf{a}_\perp|}{\sqrt{2}c} \right)^2. \end{aligned} \quad (23)$$

In the paraxial limit, the terms proportional to β can be neglected and the signal photon has the structure of a zeroth order BG photon. Outside of the paraxial limit the CAS function becomes anisotropic: there is a dependence on $\mathbf{k}_\perp^{s,i} \cdot \mathbf{a}_\perp$ arising from the moduli $|\mathbf{k}_\perp^{s,i} - \frac{n_o \omega^p}{2c} \beta \mathbf{a}_\perp|^2$. Taking a given value $\mathbf{k}_{\perp 0}^i$ for the idler transverse wavevector we find that the CAS is maximal on a contour defined by the following condition

$$\begin{aligned} \left| \mathbf{k}_\perp^s - \frac{n_o \omega^p}{2c} \beta \mathbf{a}_\perp \right|^2 \approx 2r_{AS}^2 + \kappa_\perp^2 \\ + \left(\frac{n_o \omega^p \beta |\mathbf{a}_\perp|}{\sqrt{2}c} \right)^2 - \left| \mathbf{k}_{\perp 0}^i - \frac{n_o \omega^p}{2c} \beta \mathbf{a}_\perp \right|^2 \end{aligned} \quad (24)$$

Similarly, taking fixed values for k_{y0}^s and k_{x0}^i , the $x-y$ TWC functions are maximal around

$$\begin{aligned} & \left(k_x^s - \frac{n_o\omega^p}{2c}\beta a_x\right)^2 + \left(k_y^i - \frac{n_o\omega^p}{2c}\beta a_y\right)^2 \approx 2r_{AS}^2 + \kappa_\perp^2 \\ & + \left(\frac{n_o\omega^p\beta|\mathbf{a}_\perp|}{\sqrt{2c}}\right)^2 - \left(k_{y0}^s - \frac{n_o\omega^p}{2c}\beta a_y\right)^2 + \left(k_{x0}^i - \frac{n_o\omega^p}{2c}\beta a_x\right)^2. \end{aligned} \quad (25)$$

For studying the structure of the $y-y$ and $x-x$ TWC functions, it results more convenient to write the $\Delta k_z = 0$ condition as

$$\mathbf{k}_\perp^s \cdot \mathbf{k}_\perp^i + r_{AS}^2 + \frac{n_o\omega^p\beta}{2c}\mathbf{a}_\perp \cdot (\mathbf{k}_\perp^s + \mathbf{k}_\perp^i) \approx 0, \quad (26)$$

so that we expect the TWC functions to be maximal on contours given by hyperbolae, defined by

$$k_y^s k_y^i \approx -r_{AS}^2$$

$$-k_{x0}^s k_{x0}^i - \frac{n_o\omega^p\beta}{2c} \left(a_x(k_{x0}^s + k_{x0}^i) \mp a_y \sqrt{\kappa_\perp^2 - (k_{x0}^s + k_{x0}^i)^2} \right). \quad (27)$$

In Eq. 27 the sign of the last term is positive (negative) for $k_y^s + k_y^i$ negative (positive). As a consequence, we expect that the maximal $y-y$ correlations lie on the intersection of the pair of lines mentioned in the previous subsection which result from the transverse phasematching constraint, and the hyperbolae defined by Eq. (27), which result from the longitudinal phasematching constraint. Note that for visualizing this intersection it is helpful to consider the structure of the angular spectrum, since it describes the region where the idler and signal photons can be emitted. For instance, the regions nearby the circumferences described in items (a) and (b), and the parallel lines described in (c) and (d) should overlap with the regions nearby the cones where the angular spectrum is maximal.

In order to make the asymmetry in the TWC functions, which arises from the direction of the optic axis, even more evident let us give the explicit expressions of the $k_y^s k_y^i$ and $k_x^s k_x^i$ phasematching conditions when \mathbf{a}_\perp is parallel to the x axis:

$$\begin{aligned} k_y^s k_y^i & \approx -r_{AS}^2 - k_{x0}^s k_{x0}^i - a_\perp \frac{n_o\omega^p\beta}{2c} (k_{x0}^s + k_{x0}^i) \\ k_x^s k_x^i & \approx -r_{AS}^2 - k_{y0}^s k_{y0}^i \mp a_\perp \frac{n_o\omega^p\beta}{2c} \sqrt{\kappa_\perp^2 - (k_{y0}^s + k_{y0}^i)^2}. \end{aligned}$$

Note that the analysis in this and in the previous subsections is based on the fulfilment of *perfect* transverse and longitudinal phasematching conditions, yielding contours (with zero thickness) on the transverse wavevector spaces. Under realistic experimental conditions, the full conditional angular spectrum and transverse wavevector correlation functions exhibit a width which depends on the crystal length L and BG cone pump width δ_{κ_\perp} . The expected full CAS and TWC functions, including these widths, may be obtained theoretically by direct plotting of $|F(\mathbf{k}_\perp^s, \omega^s, \mathbf{k}_\perp^i, \omega^p - \omega^s)|^2$ (see for example, Fig. 8 below), and may likewise be appreciated from our experimental measurements (see below).

III. EXPERIMENT

Our experiment exploits a spontaneous parametric downconversion photon-pair source based on a β -barium-borate (BBO) crystal in a type-I, frequency-degenerate phasematching configuration. We have used as pump zeroth order BG beams and report two different, contrasting values of the κ_\perp parameter which defines the transverse extent of the pump angular spectrum.

The pump beam preparation was accomplished in three steps (see Fig. 1). The beam from a diode laser (DL, $\lambda_p = 406.7\text{nm}$ with $\sim 70\text{mW}$ power) was first transmitted through a telescope (T1) built from lenses (L1 and L2) with focal lengths $f_1 = 5\text{cm}$ and $f_2 = 50\text{cm}$, so as to magnify the beam by a factor of $10\times$. Second, the magnified beam was transmitted through an axicon (A), placed at a distance of 10cm from lens L2, with apex angle of either 1° or 2° ; the axicons were manufactured by Altechna. Third, the beam was propagated through a second telescope (T2) built from lenses (L3 and L4) with focal lengths $f_3 = 10\text{cm}$, and either $f_4 = 15\text{cm}$ or $f_4 = 30\text{cm}$. Note that lens L3 is placed one focal length distance f_3 from a specific plane separated by either $\sim 24\text{cm}$ or $\sim 4.5\text{cm}$ from the axicon apex on which a high-quality Bessel-Gauss beam could be observed with a CCD camera (DCU224M from Thorlabs). The purpose of the second telescope is to magnify the resulting Bessel-Gauss beam so as to define the value of the κ_\perp parameter.

We have selected two different pump configurations, as stated above, each with different values of the κ_\perp parameter. These two configurations are obtained, as indicated in Table 1, by appropriate combinations of two different choices of axicon, and two different choices of focal lengths in telescope T2. The two parameters which characterize the pump beam, i. e. the BG cone radius κ_\perp and the Gaussian transverse envelope width δ_{κ_\perp} , are determined as best-fit parameters from a measurement of the angular spectrum for each of the two configurations. Note that while the resulting values of δ_{κ_\perp} are similar in the two configurations, the parameter κ_\perp exhibits a large contrast, with $\kappa_\perp = 0.0195\ \mu\text{m}^{-1}$ for configuration 1 and $\kappa_\perp = 0.147\ \mu\text{m}^{-1}$ for configuration 2. In the first row of Fig. 2, we show the measured pump angular spectrum for these two configurations along with an intermediate configuration with $\kappa_\perp = 0.045\ \mu\text{m}^{-1}$ (with increasing value of κ_\perp from left to right).

We have used a BBO crystal (from Castech) with length $L = 1\text{mm}$ and phasematching angle $\theta_{pm} = 29.3^\circ$, in order to produce frequency-degenerate, non-collinear SPDC photon pairs centered at 813.7nm . We have used two filters (F1 and F2) following the crystal, see Fig. 1: a longpass edge filter (LP02-488RS-25 from Semrock) which transmits wavelengths $\lambda > 488\text{nm}$ in order to suppress the pump, and a bandpass filter (FBH810-10 from Thorlabs) centered at 810nm with a bandwidth of 10nm so as to restrict the bandwidth of the photon pairs.

The signal and idler photons are transmitted through

configuration	κ_{\perp} [μm^{-1}]	$\delta_{\kappa_{\perp}}$ [μm^{-1}]	apex [$^{\circ}$]	second telescope (T2)
				(magnification, focal lengths for L3 and L4)
1	0.0195	0.00076	1	$3\times, f_3 = 10 \text{ cm}, f_4 = 30 \text{ cm}$
2	0.147	0.0008	2	$1.5\times, f_3 = 10 \text{ cm}, f_4 = 15 \text{ cm}$

TABLE I. For configurations 1 and 2, we show the parameters for the BG pump beam, κ_{\perp} and $\delta_{\kappa_{\perp}}$ (second and third columns), obtained through a fit of the measured pump angular spectra (first row of Fig. 2) to $|\psi(\mathbf{k}_{\perp}^{\text{p}})|^2$ (see Eq. 3). In this table we have also indicated the axicon apex angle (fourth column) and the parameters for the second telescope (T2) (fifth column). The notation coincides with that used in Fig. 1.

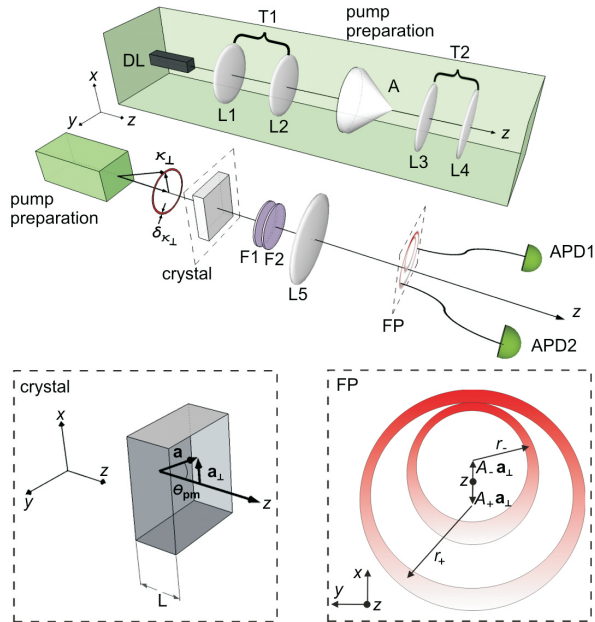


FIG. 1. Experimental setup. Back: beam preparation apparatus. Front: photon pair generation and measurement. Left-hand inset: schematic of the nonlinear crystal indicating the orientation of the optic axis. Right-hand inset: schematic of the SPDC angular spectrum, as resolved on the Fourier plane.

a lens (L5) with focal length $f_5 = 5\text{cm}$, placed at a distance f_5 from the crystal which defines a Fourier plane (FP) at a further distance f_5 from the lens. Each point on the plane FP corresponds to a specific transverse wavevector value, so that a pair of displaceable ideal point-like detectors on this plane, set to record counts in coincidence, may be used to obtain a measurement of $|F(\mathbf{k}_{\perp}^{\text{s}}, \omega^{\text{s}}, \mathbf{k}_{\perp}^{\text{p}}, \omega^{\text{p}} - \omega^{\text{s}})|^2$, as a function of any two of the four transverse wavevector components, while the other two are kept constant. Let us note that throughout this paper, the coordinate system is chosen so that z is defined by the propagation of the pump and the zy plane is parallel to the optical table; the walkoff in the nonlinear crystal occurs on the xz plane.

We have taken three different types of spatially-resolved measurements on the FP plane. First, monitoring the number of counts per unit time recorded as a function of the position of a single detector on FP, we were able to measure the marginal SPDC angular spec-

trum, i. e., the SPDC angular spectrum. Second, fixing one detector at a certain location on FP, corresponding to wavevector $\mathbf{k}_{\perp 0}$, and monitoring the counts measured in *coincidence* with a second detector as a function of the position of this second detector on FP, we obtained the conditional angular spectrum. Third, we measured signal-idler transverse wavevector correlations by monitoring the coincidence counts as a function of the position (along the x or y axes) of one detector, *and* the position (likewise along the x or y axes) of the second detector.

For measuring the AS, we placed an intensified charge-coupled device (ICCD) camera (iStar DH334T-18-F-73 from Andor), which is sensitive at the single photon level in each of 1024×1024 pixels, on the plane FP. We have measured the AS for configurations 1 and 2 of the pump, with transverse pump wavevector values of $\kappa_{\perp} = 0.0195 \mu\text{m}^{-1}$ and $\kappa_{\perp} = 0.147 \mu\text{m}^{-1}$, respectively, and in addition for an intermediate configuration with $\kappa_{\perp} = 0.045 \mu\text{m}^{-1}$. The results are presented in the second row of Fig. 2, along with corresponding simulations, obtained by numerical integration of Eq. (8) in the third row; note the excellent agreement between the numerical simulations and our measurements. Note, also, that while the smallest value of κ_{\perp} leads to an AS which is very similar to the one that would be expected for a type-I SPDC source with a paraxial Gaussian-beam pump, the AS for the largest κ_{\perp} value exhibits a dual ring structure with a high degree of azimuthal asymmetry. Note that this structure is qualitatively different from that generated by a highly-focused Gaussian-beam pump, which exhibits a *single*, azimuthally-asymmetric ring [30–32].

For the particular experimental situations considered in this paper, the radii and centers of the emission cones inferred from our experimental measurements exhibit a reasonable agreement with the corresponding values obtained from the theoretical expressions given in Section II.A. The formalism predicts, for $\kappa_{\perp} = 0.0195 \mu\text{m}^{-1}$ (configuration 1, which may be considered essentially paraxial), an angular spectrum radius of $r_{\text{AS}} = 0.484 \mu\text{m}^{-1}$ with width parameter of $\Delta_{\text{AS}} = \sigma_{\text{AS}}/r_{\text{AS}} = 0.081 \mu\text{m}^{-1}$; note that we have relied on the Sellmeier expressions for the BBO electric susceptibilities in computing these predictions. The corresponding values inferred from measurements are $\tilde{r}_{\text{AS}} = 0.473 \mu\text{m}^{-1}$ and $\tilde{\Delta}_{\text{AS}} = 0.080 \mu\text{m}^{-1}$. For the case $\kappa_{\perp} = 0.147 \mu\text{m}^{-1}$ (configuration 2, which departs from the paraxial regime), the theoretical radii of the two emission cones in wavevector space are $r_{+} = 0.55 \mu\text{m}^{-1}$

and $r_- = 0.27 \mu\text{m}^{-1}$, with their centers located at $A_{\pm} = \mp 0.1 \mu\text{m}^{-1}$ along \mathbf{a}_{\perp} . From our measurements we may infer the corresponding values $\tilde{r}_+ = 0.58 \mu\text{m}^{-1}$, $\tilde{r}_- = 0.30 \mu\text{m}^{-1}$, and $\tilde{A}_{\pm} = \mp 0.1 \mu\text{m}^{-1}$. These results are summarized in Table II.

Note that there are a number of factors which contribute to determine the observed widths of the SPDC emission cones. First, the parameter σ_{AS} in Eq. (9) is highly dependent on the crystal length L ; in addition, while Eq. (9) assumes $\delta_{\kappa_{\perp}} \rightarrow 0$, the BG cone width $\delta_{\kappa_{\perp}}$ also influences the width of the SPDC cones. Second, while the theoretical description assumes that the pump is normally-incident, unavoidable small tilts in the experiment may also contribute. Third, while the form of the theory presented here assumes ideal spectral filters of zero width applied to the signal and idler photon pairs, the actual width of the spectral filters used (10nm) also has an important effect. In the numerical simulations all these factors can be incorporated, in particular distributions (e.g. described by Gaussian functions), introduced so as to describe both the spectral filtering and the pump spectral envelope [30, 34]. The simulations show that a tilt between the incident pump and the normal to the crystal surface (while leaving the crystal cut angle fixed) of less than 0.2° is enough to surmount almost completely the slight discrepancies between Figs. 2 (e) and (h), and (f) and (i). Let us emphasize that Figs. 2 (g-i) illustrate the predictions of the ideal model described in Section II.B (which excludes such tilting) and from which the parameters shown in Table II were obtained.

For measuring the CAS, we placed the fiber tips of two different multimode fibers (with $64 \mu\text{m}$ core radius) on the FP plane, each fiber leading to a Si avalanche photodiode (APD). Each of the two fiber tips was mounted so that it could be displaced on the FP plane with the help of two computer-controlled linear micro-translation stages (M-111.1DG from Physik Instrumente, with 50nm resolution and 1.5cm travel). A given position on FP of the idler-mode fiber tip, corresponding to wavevector value \mathbf{k}_{\perp}^i is then selected and the signal-mode fiber tip is scanned around the position corresponding to the transverse wavevector $-\mathbf{k}_{\perp}^i$, while monitoring coincidence counts between the signal and idler photons.

We set out to compare measurements of the CAS performed for our two different pump beam configurations. In order to test the azimuthal distinguishability of the two-photon state, we selected five different positions of the idler-mode fiber tip around the upper half of the angular spectrum. In Fig. 3 we show— for pump configuration 1—the angular spectrum along with the five selected idler detector locations, labelled i, ii, iii, iv, and v. We also show, superimposed on the plot of the AS, plots for the CAS function measured for each of these points, each labelled with the corresponding primed Roman numeral. While in this plot the relative locations with respect to the AS of these five different CAS functions can be appreciated clearly, we also show in five additional panels each of the CAS measurements for easier visualization of

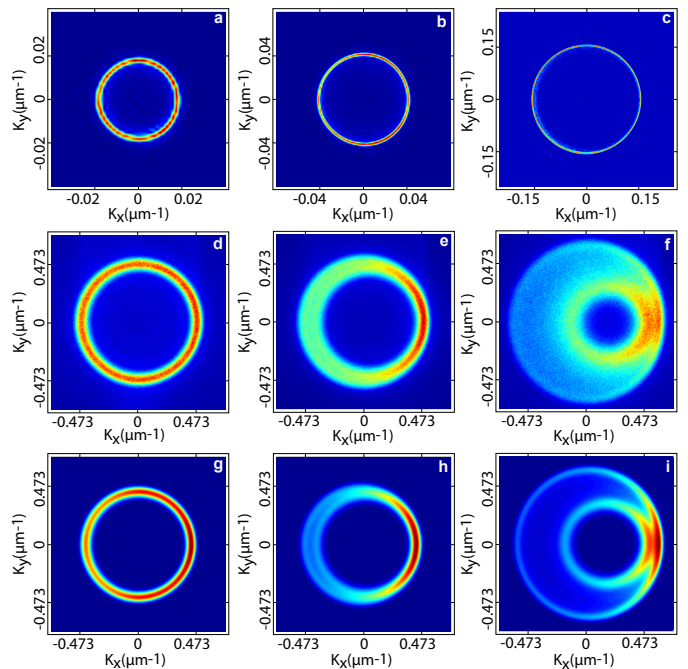


FIG. 2. For pump configurations 1 (first column), 2 (third column), along with an intermediate configuration (second column), we show the following: in the first row, the measured angular spectrum of the pump, in the second row the measured SPDC angular spectrum obtained through spatially-resolved, single-channel photon counting on the Fourier plane, and in the third row: simulated SPDC angular spectrum using the parameters from Table 1 for the first and third column.

their structure.

Note that, interestingly, the CAS exhibits essentially the same structure for the five selected positions of the idler detector. This is consistent with the relatively small value of κ_{\perp} for pump configuration 1, for which the two-photon state is determined mainly by the pump properties. In fact, as explained in Section II.B, in this case the CAS has a similar structure to the pump angular spectrum, except for a transverse displacement according to the position of the idler detector. This is a consequence of the fact that for a sufficiently small value of κ_{\perp} (in combination with a sufficiently thin crystal) the width of the function $\mathcal{L}(k_{\perp}^s, k_{\perp}^i)$ — see Eq. (18) — is considerably less than that of the function $\mathcal{L}(k_{\perp}^s, k_{\perp}^i)$ — see Eq. (19) — so that the former dominates. Note that the fact that the CAS has an unchanging structure around the AS leads to the azimuthal symmetry (i. e. single SPDC ring with constant width) of the AS.

Let us now compare this behavior with that resulting from pump configuration 2, which is characterized by a much larger value of κ_{\perp} . In this case, we have likewise selected five positions for the idler detector around the SPDC angular spectrum, labelled as i, ii, iii, iv, and v, in the large panel of Fig. 4. We also show superimposed on the SPDC angular spectrum, as we did for configuration 1, the CAS corresponding to each of these idler detector

Configuration	Theory	Experiment
$\kappa_{\perp} = 0.0195 \mu\text{m}^{-1}$	$r_{AS} = 0.484 \mu\text{m}^{-1}$	$\tilde{r}_{AS} = 0.473 \mu\text{m}^{-1}$
$\kappa_{\perp} = 0.0195 \mu\text{m}^{-1}$	$\Delta_{AS} = 0.081 \mu\text{m}^{-1}$	$\tilde{\Delta}_{AS} = 0.080 \mu\text{m}^{-1}$
$\kappa_{\perp} = 0.147 \mu\text{m}^{-1}$	$r_{+} = 0.55 \mu\text{m}^{-1}$	$\tilde{r}_{+} = 0.58 \mu\text{m}^{-1}$
$\kappa_{\perp} = 0.147 \mu\text{m}^{-1}$	$r_{-} = 0.27 \mu\text{m}^{-1}$	$\tilde{r}_{-} = 0.30 \mu\text{m}^{-1}$
$\kappa_{\perp} = 0.147 \mu\text{m}^{-1}$	$A_{\pm} = \mp 0.1 \mu\text{m}^{-1}$	$\tilde{A}_{\pm} = \mp 0.1 \mu\text{m}^{-1}$

TABLE II. Comparison between the experimental and expected parameters describing the angular spectra of SPDC with Bessel-Gauss pump beams. In the paraxial regime, illustrated by a pump beam with $\kappa_{\perp} = 0.0195 \mu\text{m}^{-1}$, the emission cone is expected to have an r_{AS} radius in wavevector space given by Eq. (10), and a width $\Delta_{AS} = \sigma_{AS}/r_{AS}$ with σ_{AS} given by Eq. (11). Outside this regime, illustrated by a pump beam with $\kappa_{\perp} = 0.147 \mu\text{m}^{-1}$, two non-collinear cones exhibit radii given by r_{\pm} , Eq. (14) and are centered at A_{\pm} , Eq. (15).

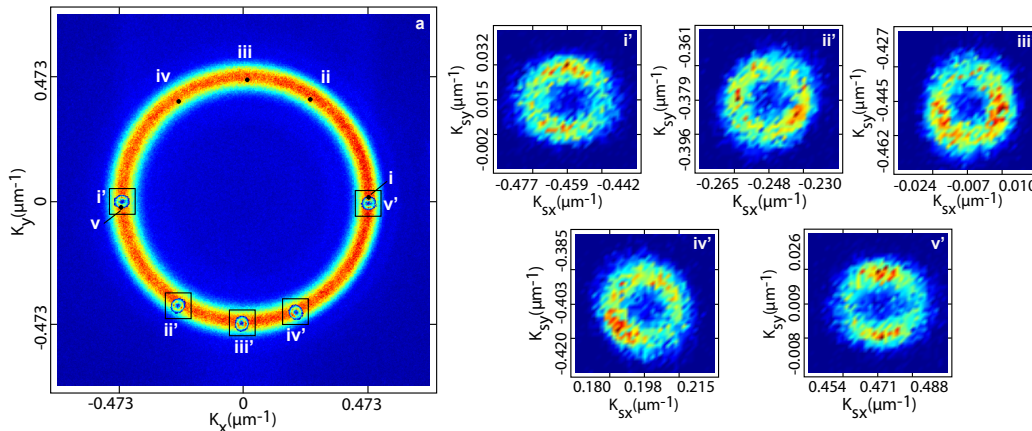


FIG. 3. (a) SPDC angular spectrum for pump configuration 1 (also shown in Fig. 2d), in which we have indicated 5 different locations distributed around the upper circumference of the SPDC angular spectrum, labelled as (i) through (v), of the fixed conditioning detector along with the corresponding conditional angular spectrum (CAS) appearing in the diametrically opposed portion of the ring, labelled as (i') through (v'). In each of panels (i') through (v') we have shown the CAS for each of the fixed conditioning detector positions (i) through (v), in individual plots for enhanced clarity.

positions, each labelled with the corresponding primed Roman numeral; in addition, we have presented in five additional panels each of the CAS measurements for easier visualization of its structure. It is no surprise that each CAS function covers a larger area of the transverse wavevector space, as compared to configuration 1, since the CAS transverse extent is ‘inherited’ from the pump angular spectrum. More interestingly, in this case the CAS function leads to signal photons that have a conditional angular spectrum which differs significantly from that of a Bessel-Gauss photon. The resulting azimuthal angular structure in the transverse wavevector space can be written as a superposition of $\cos(n\varphi_{\mathbf{k}})$ functions (that would be related to stationary Bessel-Gauss photons [22]) or Mathieu $ce_n(\varphi_{\mathbf{k}})$ functions (that would be related to stationary Mathieu photons [33]). This effect is a consequence of the fact that the $\mathcal{S}(k_{\perp}^s, k_{\perp}^i)$ function is now much wider as compared to configuration 1, to the extent that the function $\mathcal{L}(k_{\perp}^s, k_{\perp}^i)$ (which does not depend on the pump spatial structure) now clips the displaced pump angular spectrum in a different manner at each location of the SPDC angular spectrum.

In order to further study the anisotropy induced by the

direction of the optic axis on the CAS, we show in Fig. 5 our measurement of the CAS for pump configuration 2, for three different positions labelled as i, ii, and iii, of the idler detector across the right flank of the SPDC ring. It becomes clear that as we displace the idler detector, different portions of the $\mathcal{S}(k_{\perp}^s, k_{\perp}^i)$ function, which has an annular structure, are revealed.

In order to measure the signal-idler transverse wavevector correlations we use the same setup as was used for measuring the CAS function. First, we choose two reference locations on the FP plane for the signal and idler detectors, around which the detectors will be displaced. Second, we choose directions of detector displacement, x or y , for each of the signal and idler detectors. Third, for each position of the signal detector, we scan the idler detector along the full range permitted. In this manner, we build a matrix of coincidence counts corresponding to different combinations of positions, along the selected directions and around the selected reference locations, for the two detectors.

In the large panel of Fig. 6 we show a contour plot of the SPDC angular spectrum, for pump configuration 1, and show two pairs of axes with their respective ori-

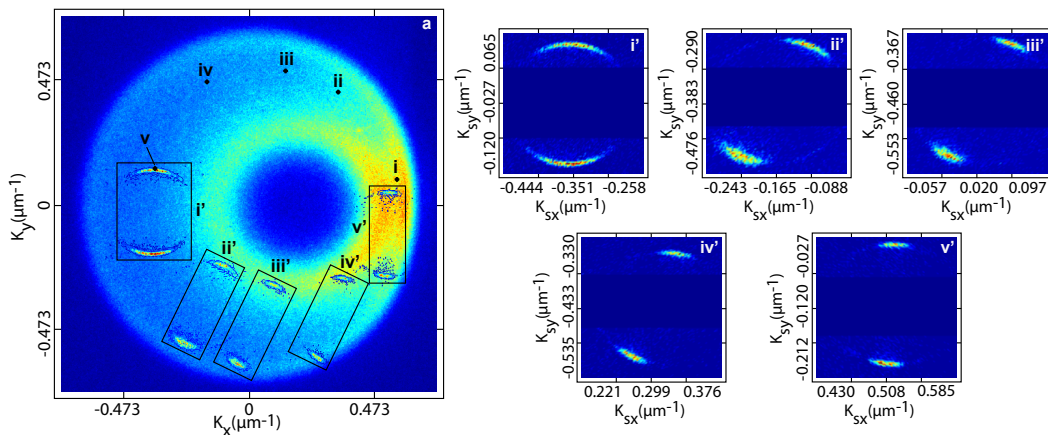


FIG. 4. (a) SPDC angular spectrum for pump configuration 2 (also shown in Fig. 2f), in which we have indicated 5 different locations distributed around the upper circumference of the SPDC angular spectrum, labelled as (i) through (v), of the fixed conditioning detector along with the corresponding conditional angular spectrum (CAS) appearing in the diametrically opposed portion of the ring, labelled as (i') through (v'). In each of panels (i') through (v') we have shown the CAS for each of the fixed conditioning detector positions (i) through (v), in individual plots for enhanced clarity.

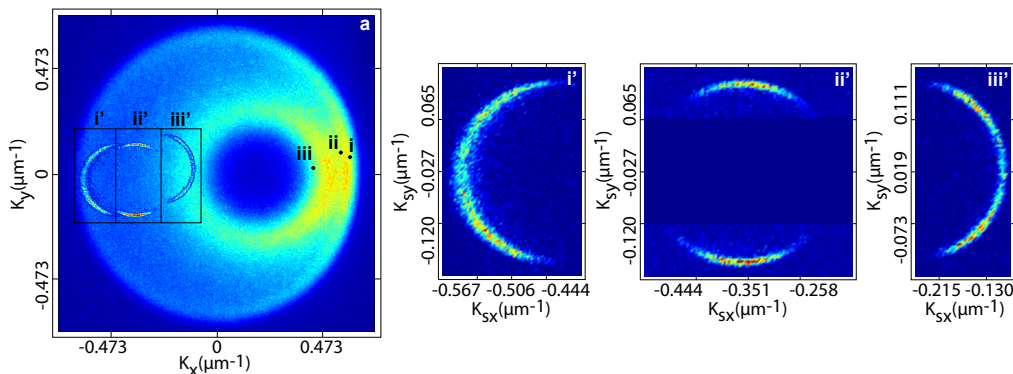


FIG. 5. (a) SPDC angular spectrum for pump configuration 2 (also shown in Fig. 2f), in which we have indicated 3 different locations distributed radially on the right-hand-side of the SPDC angular spectrum, labelled as (i) through (iii), of the fixed conditioning detector along with the corresponding conditional angular spectrum (CAS) appearing in the diametrically opposed portion of the ring, labelled as (i') through (iii'). In each of panels (i') through (iii') we have shown the CAS for each of the fixed conditioning detector positions (i) through (iii), in individual plots for enhanced clarity.

gins indicating the selected reference locations. While in the top row of smaller panels we show our measurements of the $x-x$, $y-y$, and $x-y$ TWC functions, in the second row we show corresponding simulations obtained from numerical integration of Eq. (8). It is notable that there is excellent agreement between theory and experiment. As discussed in Section II.B, the most striking difference with respect to similar measurements that would be obtained for a standard Gaussian-beam pump [35], is that both $x-x$ and $y-y$ correlations become “double correlations” in the sense that the diagonal region with non-zero coincidence counts becomes, for a Bessel-Gauss beam, duplicated.

Note that the $x-y$ TWC function measurement reveals a structure which is essentially that of the pump angular spectrum, as expected from the discussion in Sec-

tion II.B. Note also that the $y-y$ TWC function measurements yields significantly longer coincidence count regions as compared to the $x-x$ TWC function measurements. This is because while the y direction is tangent to the SPDC angular spectrum, the x direction cuts radially through the angular spectrum. It is interesting that the same source can yield very different degrees of correlation according to whether detectors are scanned in the x or y directions. Note that it becomes possible to scan the detectors in rotated x and y axes with the possibility of continuously tuning between the two extremes of shorter $x-x$ and longer $y-y$ correlations, as controlled by the axis rotation. This represents an interesting added versatility of this type of source.

Let us now compare this behavior with that resulting for pump configuration 2. The large panel in Fig. 7

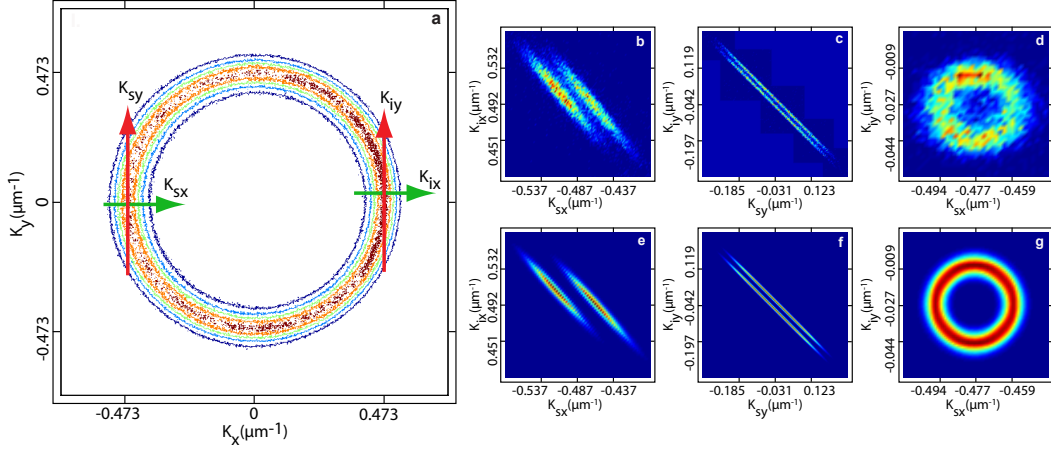


FIG. 6. (a) SPDC angular spectrum for pump configuration 1 (also shown in Fig. 2d), on which we have indicated (origins of the two sets of red-colored axes) the central locations from which we scan the signal and idler detectors for our $x-x$, $y-y$ and $x-y$ transverse wavevector correlation measurements. In panels (b), (c), and (d) we have shown our measured $x-x$, $y-y$, and $x-y$ transverse wavevector correlations. In panels (e), (f), and (g) we have shown corresponding simulations for each of the $x-x$, $y-y$ and $x-y$ correlations.

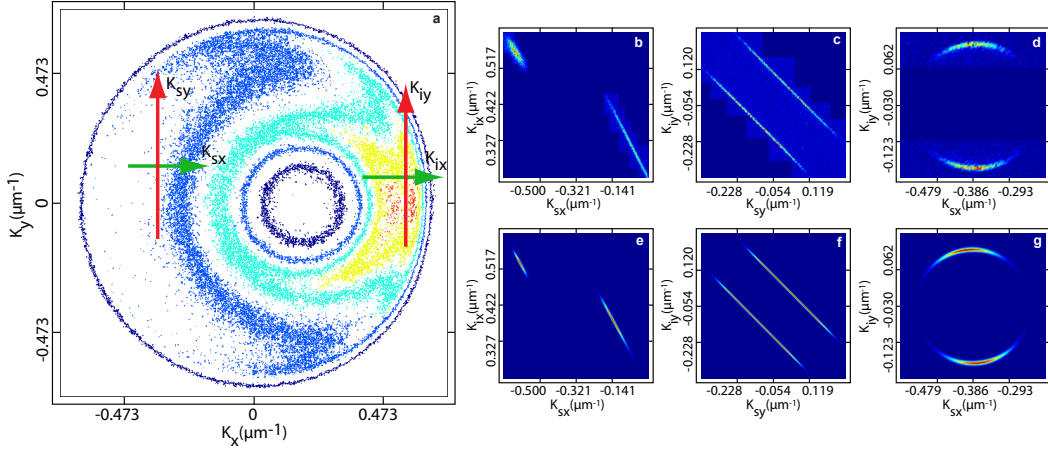


FIG. 7. (a) SPDC angular spectrum for pump configuration 2 (also shown in Fig. 2), on which we have indicated (origins of the two sets of red-colored axes) the central locations from which we scan the signal and idler detectors for our $x-x$, $y-y$ and $x-y$ transverse wavevector correlation measurements. In panels (b), (c), and (d) we have shown our measured $x-x$, $y-y$, and $x-y$ transverse wavevector correlations. In panels (e), (f), and (g) we have shown corresponding simulations for each of the $x-x$, $y-y$ and $x-y$ correlations.

shows a contour plot of the SPDC spectrum, and as for the previous case, the origins of the two sets of shown axes indicate the two chosen reference locations. While in the first row of smaller panels we have shown $x-x$, $y-y$, and $x-y$ TWC function measurements, in the second row we have indicated corresponding simulations obtained from numerical integration of Eq. (16). Note that in this case, the two coincidence count regions in the $x-x$ correlation measurement become highly unequal, and furthermore these two regions no longer overlap in k_x^s the coordinate, and essentially do not overlap in the k_x^i coordinate. This is necessarily due to dependence of the longitudinal phasematching function \mathcal{L} on the orientation of the

optic axis (in our configuration $\mathbf{a} = (a_x, 0, a_z)$). Notice also that the relevant values of k_x^s are negative while k_x^i are positive; evidently, the phasematching effective equation, Eq. (26) cannot be fulfilled for k_x^s and k_x^i with the same sign in this configuration. Also note that the $x-y$ measurement once again shows essentially the structure of the pump angular spectrum, except clipped by \mathcal{L} , for this larger value of κ_\perp as expected from Eq. (25).

In Fig. 8 we have shown, for pump configuration 2, how the structure of the transverse $x-x$, $y-y$ and $x-y$ correlations is determined by functions $\mathcal{L}(k_\perp^s, k_\perp^i)$ and $\mathcal{L}(k_\perp^s, k_\perp^i)$. The case of $x-x$ correlations (with $k_y^s = k_{y0}^s$ and $k_y^i = k_{y0}^i$) is shown in the first row. Pan-

els (a), (b), and (c) show resulting plots of the functions $\mathcal{S}(k_{\perp}^s, k_{\perp}^i)$, which contains information about the pump angular spectrum, $\mathcal{L}(k_{\perp}^s, k_{\perp}^i)$, which contains information about the crystal phasematching properties, and the product $\mathcal{S}(k_{\perp}^s, k_{\perp}^i)\mathcal{L}(k_{\perp}^s, k_{\perp}^i)$, which represents the $x-x$ TWC function. The second row is similar to the first row, except now for the case of $y-y$ correlations (with $k_x^s = k_{x0}^s$ and $k_x^i = k_{x0}^i$). It becomes evident that while function $\mathcal{S}(k_{\perp}^s, k_{\perp}^i)$ defines the doublet stripe structure, function $\mathcal{L}(k_{\perp}^s, k_{\perp}^i)$ determines the transverse extent of these stripes. The third row is similar to the previous one, illustrating now the $x-y$ correlations; while $\mathcal{S}(k_{\perp}^s, k_{\perp}^i)$ carries direct information from the pump beam, the varying magnitude along the circumference in the CAS is due to the $\mathcal{L}(k_{\perp}^s, k_{\perp}^i)$ factor.

One of the salient features of SPDC with BG pump beams is that as the value of κ_{\perp} increases, the angular spectrum of the signal and idler photon pairs becomes increasingly concentrated on the transverse wavevector plane. This effect is evident for example in Fig. 5(a), where the probability of emission is greater on the right flank of the angular spectrum. Let us note that in typical type-I SPDC sources, with an azimuthally-symmetric cone of emission, all of the flux emitted which does not correspond to two diametrically-opposed portions of the ring is effectively wasted. In this context, the breaking of azimuthal symmetry and concentration of the flux on the transverse wavevector plane could prove to be a useful resource for a boosted flux along a specific, desired direction of propagation.

In this paper we have focused our attention on the appearance of double transverse wavevector correlations. As we have discussed, the ring structure of the pump angular spectrum directly implies that the TWC function splits into characteristic doublet stripes. It is interesting to point out that a pump formed by the coherent addition of two BG beams with different values of κ_{\perp} , i. e. exhibiting a dual-ring angular spectrum, would lead to TWC functions exhibiting four instead of two stripes. Likewise, the coherent addition of a Gaussian beam and a BG beam would result in TWC functions showing three characteristic stripes. Appropriate combinations of Gaussian and BG pump modes could then result in a certain scalability in the splitting of transverse wavevector correlations [36]. One possibility would be to employ such a source in a ghost imaging setup [37, 38] so as to obtain multiple ghost images, one per stripe appearing in the TWC functions.

IV. CONCLUSIONS

The two-photon state produced by spontaneous parametric downconversion is constructed from the coherent addition of the individual contributions due to all available pump wavevectors. In this paper we have focused on the use of a Bessel-Gauss (BG) pump, which corresponds to a conical superposition of Gaussian beams;

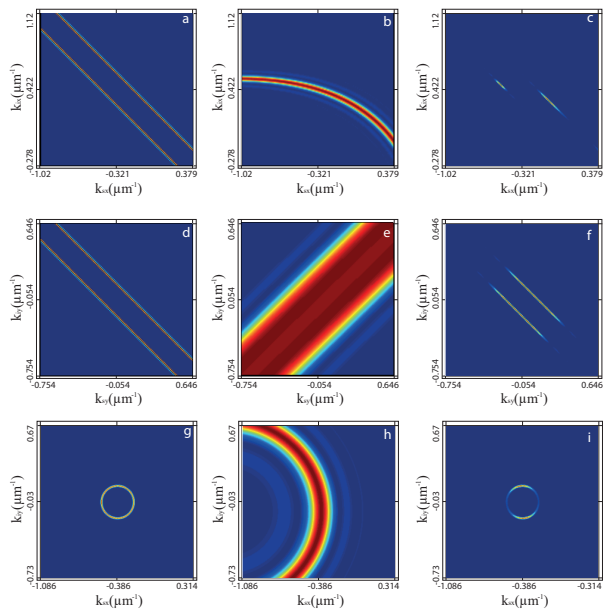


FIG. 8. In the first row we show plots of the functions $\mathcal{S}(k_{\perp}^s, k_{\perp}^i)$, panel (a), $\mathcal{L}(k_{\perp}^s, k_{\perp}^i)$, panel (b), and of the product $\mathcal{S}(k_{\perp}^s, k_{\perp}^i)\mathcal{L}(k_{\perp}^s, k_{\perp}^i)$, panel (c), for the specific case of $x-x$ wavevector correlations, with $k_{y0}^i = k_{y0}^s = 0$. In the second row we show similar plots for the case of $y-y$ transverse wavevector correlations with $k_{x0}^i = k_{x0}^s = 0$. In the third row similar plots are shown for $x-y$ transverse wavevector correlations.

we have characterized BG beams with two parameters: the transverse wavevector cone radius κ_{\perp} and its width $\delta\kappa_{\perp}$. While in our experiments we have oriented the main pump propagation axis parallel to the normal to the crystal front surface, BG pump beams imply a significant spread of pump wavevectors impinging non-symmetrically with respect to the optic axis, leading to a considerable departure from cylindrical symmetry in the two-photon state. This is reflected in a non-concentric double-cone SPDC angular spectrum, with the conditional angular spectrum exhibiting a shape which depends on the azimuthal location of the heralding detector. In addition, as the pump becomes increasingly non-paraxial (quantified by larger values of κ_{\perp}), the signal-idler wavevector correlation region splits into characteristic doublet stripes implying that each signal-photon wavevector is correlated with two distinct idler wavevectors.

We have presented a general theory which describes SPDC two-photon states involving a BG pump which can range from paraxial to highly non-paraxial. We have also presented measurements which agree extremely well with corresponding simulations based on our theory. We believe that the double transverse wavevector correlations which we have demonstrated represents an interesting new resource for photon-pair quantum state engineering.

ACKNOWLEDGMENTS

This work was supported by CONACyT LN-271322, México, by PAPIIT(UNAM) grant IN1050915, and by AFOSR grant FA9550-16-1-0458.

-
- [1] D. G. Grier, *A revolution in optical manipulation*, Photonic Technologies **424**, 810 (2003).
- [2] G. Knöner, S. Parkin, V. L. Y. Nieminen, T. A. Love, N. R. Heckenberg, and H. Rubinsztein-Dunlop, *Integrated optomechanical microelements*, Opt. Express **15**, 5521 (2007).
- [3] M. Woerdemann, C. Alpman, M. Esseling, and C. Denz, *Advanced optical trapping by complex beam shaping*, Laser Photonics Rev. **7**, 839 (2013).
- [4] M. A. Alonso, *Wigner functions in optics: describing beams as ray bundles and pulses as particle ensembles*, Advances in Optics and Photonics **3**, 272 (2011).
- [5] S. Ngcobo, I. Litvin, L. Burger, and A. Forbes, *A digital laser for on-demand laser modes*, Nat. Commun. **4**, 2289 (2013).
- [6] M. Zürch, C. Kern, P. Hansinger, A. Dreischuh, and C. Spielmann, *Strong-field physics with singular light beams*, Nat. Phys. **8**, 743 (2012).
- [7] I. Dolev, I. Kaminer, A. Shapira, M. Segev, and A. Arie, *Experimental observation of self-accelerating beams in quadratic nonlinear media*, Phys. Rev. Lett. **108**, 113903 (2012).
- [8] R. Jáuregui and J. P. Torres, *On the use of structured light in nonlinear optics studies of the symmetry group of a crystal*, Sci. Rep. **6**, 20906 (2016).
- [9] M. G. L. Gustafsson, *Nonlinear structured-illumination microscopy: Wide-field fluorescence imaging with theoretically unlimited resolution*, PNAS **102**, 13081 (2005).
- [10] J. Durnin, *Exact solutions for nondiffracting beams. I. The scalar theory*, J. Opt. Soc. Am. A **4**, 651 (1987); J. Durnin, J. J. Miceli Jr., and J. H. Eberly, *Diffracton-free beams*, Phys. Rev. Lett. **58**, 1499 (1987).
- [11] J. Arlt and K. Dholakia, *Generation of high-order Bessel beams by use of an axicon*, Opt. Commun. **177**, 297 (2000).
- [12] C. López-Mariscal, J. C. Gutiérrez-Vega, and S. Chávez-Cerda, *Production of high-order Bessel beams with a Mach-Zehnder interferometer*, Appl. Opt. **43**, 5060 (2004).
- [13] A. Mair, A. Vaziri G. Weihs, and A. Zeilinger, *Entanglement of the orbital angular momentum states of photons*, Nature **412**, 313 (2001).
- [14] G. Molina-Terriza, J. P. Torres, and L. Torner, *Twisted photons*, Nat. Phys. **3**, 305-310 (2007).
- [15] Z. Bouchal, J. Wagner, and M. Chlup, *Self-reconstruction of a distorted nondiffracting beam*, Opt. Commun. **151**, 207 (1998).
- [16] Y. Gu and G. Gbur, *Scintillation of pseudo-Bessel correlated beams in atmospheric turbulence*, J. Opt. Soc. Am. A **27**, 2621 (2010).
- [17] A. V. Burlakov, M. V. Chekhova, D. N. Klyshko, S. P. Kulik, A. N. Penin, Y. H. Shih, and D. V. Strelakov, *Interference effects in spontaneous two-photon parametric scattering from two macroscopic regions*, Phys. Rev. A **56**, 3214 (1997).
- [18] C. H. Monken, P. H. Souto Ribeiro, and S. Pádua, *Transfer of angular spectrum and image formation in spontaneous parametric down-conversion*, Phys. Rev A **57**, 3123 (1998).
- [19] H. Cruz-Ramírez, R. Ramírez-Alarcón, F. J. Morelos, P. A. Quinto-Su, J. C. Gutiérrez-Vega, and A. B. U'Ren, *Observation of non-diffracting behavior at the single photon level*, Opt. Exp. **20**, 29761 (2012).
- [20] V. Vicuña-Hernández, H. Cruz-Ramírez, R. Ramírez-Alarcón, and A. U'Ren, *Classical to quantum transfer of optical vortices*, Opt. Exp. **22**, 20027 (2014).
- [21] R. Ramírez-Alarcón, V. Vicuña-Hernández, H. Cruz-Ramírez and A. B. U'Ren, *Transverse amplitude transfer experiments based on the process of spontaneous parametric downconversion*, Phys. Scripta **90**, 068013 (2015).
- [22] Y. Jerónimo-Moreno and R. Jáuregui, *On demand generation of propagation invariant photons with orbital angular momentum*, Phys. Rev. A **90**, 013833 (2014).
- [23] S. Prabhakar, S. Gangi Reddy, A. Aadhi, A. Kumar, P. Chithrabhanu, G. K. Samanta, and R. P. Singh, *Spatial distribution of spontaneous parametric down-converted photons for higher order optical vortices*, Opt. Commun. **326**, 64 (2014).
- [24] M. V. Jabir, N. Apurv Chaitanya, A. Aadhi, and G. K. Samanta, *Generation of "perfect" vortex of variable size and its effect in angular spectrum of the down-converted photons*, Sci. Rep. **6**, 21877 (2016).
- [25] C. I. Osorio, G. Molina-Terriza, and J. P. Torres, *Correlations in orbital angular momentum of spatially entangled paired photons generated in parametric down-conversion*, Phys. Rev. A **77**, 015810 (2008).
- [26] O. Calderón-Losada, J. Flórez, J. P. Villabona-Monsalve, and A. Valencia, *Measuring different types of transverse momentum correlations in the biphotons Fourier plane*, Opt. Lett. **41**, 1165 (2016).
- [27] W. H. Peeters, J. J. Moerman, and M. P. van Exter, *Observation of Two-Photon Speckle Patterns*, Phys. Rev. Lett. **104**, 173601 (2010).
- [28] M. A. D. Carvalho, J. Ferraz, G. F. Borges, P. -L. de Assis, S. Pádua, and S. P. Walborn, *Experimental observation of quantum correlations in modular variables*, Phys. Rev. A **86**, 032332 (2012).
- [29] R. M. Gomes, A. Salles, F. Toscano, P. H. Souto Ribeiro, and S. P. Walborn, *Observation of a nonlocal optical vortex*, Phys. Rev. Lett. **103**, 033602 (2009).
- [30] R. Ramírez-Alarcón, H. Cruz-Ramírez and A. B. U'Ren, *Effects of crystal length on the angular spectrum of spontaneous parametric downconversion photon pairs*, Laser Phys. **23**, 055204 (2013).
- [31] Y. Jerónimo-Moreno and R. Jáuregui, *Type I parametric down conversion of highly focused Gaussian beams in finite length crystals*, J. Opt. **16** 065201 (2014).
- [32] M. V. Fedorov, *Azimuthal entanglement and multichan-*

- nel Schmidt-type decomposition of non-collinear biphotons*, Phys. Rev. A **93**, 033830 (2016).
- [33] R. Hernandez-Aranda and J. C. Gutiérrez-Vega, *Focal shift in vector Mathieu-Gauss beams*, Opt. Exp. **16**, 5838 (2008).
- [34] C. J. Pugh, P. Kolenderski, C. Carcella, A. Jennewein, *Towards correcting atmospheric beam wander via pump beam control in a down conversion process*, Opt. Express **24**, 20947 (2016).
- [35] M.P. Edgar, D.S. Tasca, F. Izdebski, R.E. Warburton, J. Leach, M. Agnew, G.S. Buller, R.W. Boyd, and M.J. Padgett, *Imaging high-dimensional spatial entanglement with a camera*, Nat. Comm. **3**, 984 (2012).
- [36] A. R. Altman, K. G. Köprülü, E. Corndorf, P. Kumar, and G. A. Barbosa, *Quantum imaging of nonlocal spatial correlations induced by orbital angular momentum*, Phys. Rev. Lett **94**, 123601 (2005).
- [37] D. V. Strekalov, A. V. Sergienko, D. N. Klyshko, and Y. H. Shih, *Observation of two-photon ghost interference and diffraction*, Phys. Rev. Lett. **74**, 3600 (1995).
- [38] T. B. Pittman, Y. H. Shih, D. V. Strekalov, and A. V. Sergienko, *Optical imaging by means of two-photon quantum entanglement*, Phys. Rev. A **52**, R3429 (1995).